Asymmetric nanoparticle may go "active" at room temperature

Article

Accepted Version

Sheng, N., Tu, Y., Guo, P., Wan, R., Wang, Z. and Fang, H. (2017) Asymmetric nanoparticle may go "active" at room temperature. Science China Physics, Mechanics & Astronomy, 60 (4). 040511. ISSN 1869-1927 doi: https://doi.org/10.1007/s11433-016-9001-x Available at http://centaur.reading.ac.uk/69289/

Asymmetric Nanoparticle May Go "Active" at Room Temperature

Nan Sheng[1], YuSong Tu[2], Pan Guo[1], RongZheng Wan[1], ZuoWei Wang[3*], and HaiPing Fang[1*]

[1] *Division of Interfacial Water and Key Laboratory of Interfacial Physics and Technology, Shanghai Institute of Applied Physics, Chinese Academy of Sciences, P.O. Box 800-204, Shanghai 201800, China*

[2] *College of Physics Science and Technology, Yangzhou University, Jiangsu, 225009, China*

[3] *School of Mathematical, Physical and Computational Sciences, University of Reading, Whiteknights, Reading RG6 6AX, United Kingdom*

*Corresponding authors (email: fanghaiping@sinap.ac.cn; zuowei.wang@reading.ac.uk)

Using molecular dynamics simulations, we show that an asymmetrically shaped nanoparticle in dilute solution possesses a spontaneously curved trajectory within a finite time interval, instead of the generally expected random walk. This unexpected dynamic behavior has a similarity to that of active matters, such as swimming bacteria, cells, or even fish, but is of a different physical origin. The key to the curved trajectory lies in the non-zero resultant force originated from the imbalance of the collision forces acted by surrounding solvent molecules on the asymmetrically shaped nanoparticle during its orientation regulation. Theoretical formulae based on microscopic observations have been derived to describe this non-zero force and the resulting motion of the asymmetrically shaped nanoparticle.

1 Introduction

The motion of molecules caused by thermal fluctuations, as one of the most fundamental forms of mass, momentum and energy transport in nature, plays an essential role in many physical processes [1–4], chemical reactions [5–7] and biological functions [8–14]. In conventional theories, molecules/particles have been treated as perfect spheres with their trajectories described as random walks, following the original work of Einstein [15–18]. However, it has been realized by Einstein himself that this picture will break down if we can inspect the motion of the particles at sufficiently small time and length scales [9]. Significant progress has been made in investigating the motion of particles at the micrometer scale and timescales from microseconds to seconds, revealing that particles show unconventional behavior over relatively short time intervals [19–21]. Han et al. [19] experimentally observed a crossover from short-time anisotropic to long-time isotropic diffusion behavior of ellipsoidal particles along different axial directions. Huang and colleagues experimentally measured the mean-square displacement of a silica sphere with a diameter of 1 μm in water using an optical trapping technique and found that the particle motion could not be described by conventional theory until after a sufficiently long time [21]. We note that, a majority of kinetic and dynamic processes related to molecules take place in nanoscale space [8–11,22–25] and are accomplished in just several picoseconds [26,27], such as self-assembly [3,4,28–30], chemical reaction initiation [5–7,31], intercellular signal transduction [32–34], and neurotransmission [34,35]. Unfortunately, there is rare report on the unconventional behavior of the free motion of molecules/nanoparticles solely under thermal fluctuations within short time at the nanoscale.

On the other hand, molecular dynamics (MD) simulation has been widely accepted as a powerful tool for studying the dynamics of molecules at nanoscales [36–45]. Our recent atomistic MD simulations showed interesting anisotropic motion of small asymmetric solute molecules, such as methanol and glycine, in water solely caused by thermal fluctuations [46,47], which indicates the existence of rich dynamic behavior of asymmetric molecules in nano-space at finite timescales.

In this work, we report the emergence of unexpected spontaneous curvature in the trajectory of an asymmetrically shaped nanoparticle in dilute solution, rather than a random walk. This curvature results from a non-zero resultant force, which originates from the imbalance of the collision forces acted by surrounding solvent molecules on the asymmetrically shaped nanoparticle. The spontaneously curved trajectory of the asymmetrically shaped particle, together with the non-zero

orientation-dependent force from the surrounding solvent, is similar to the behavior of active matters, like swimming bacteria, cells, or even fish. However, different from the self-propelled active matter that consumes energy to generate driving force, the non-zero resultant force experienced by the asymmetrically shaped particle solely results from collisions with the surrounding solvent during its orientation regulation under thermal fluctuations. Further, we derive theoretical formulae based on the observed microscopic picture that can well describe the non-zero force and resulting motion of the nanoparticle.

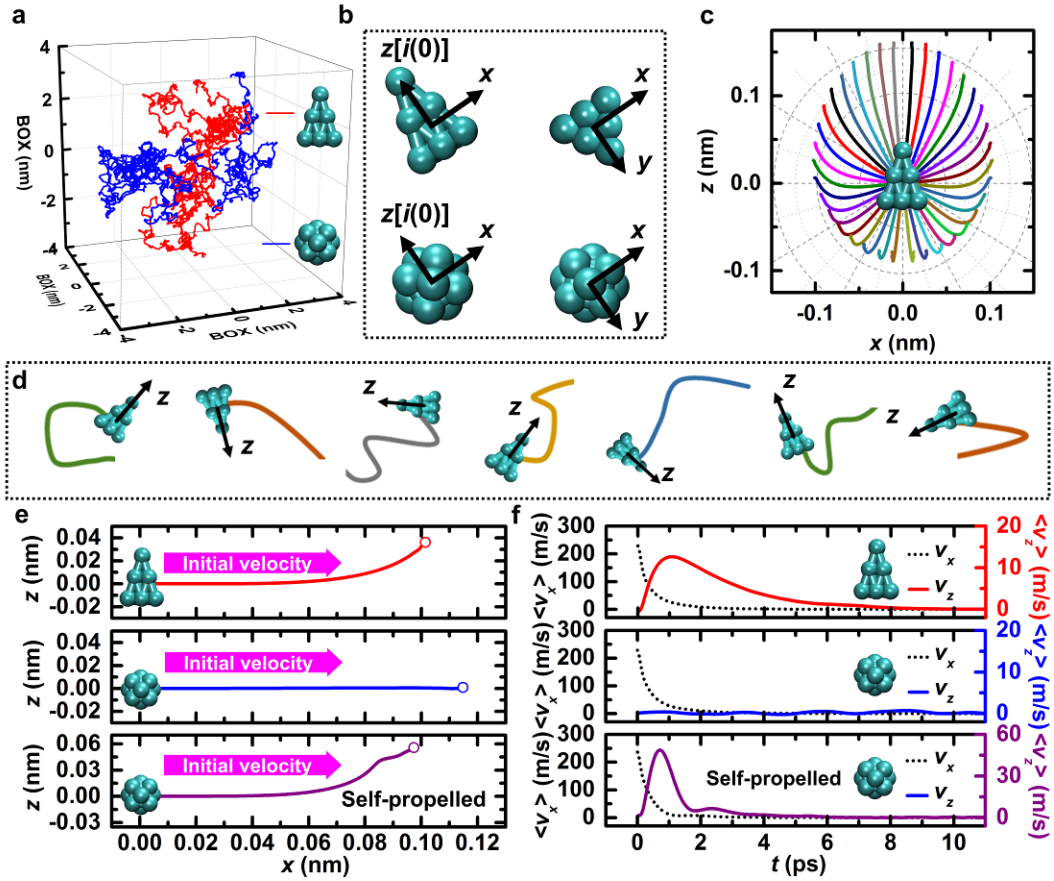

Figure 1 (a) Typical trajectories of a pyramid-shaped nanoparticle with height of 0.37 nm and a spherical nanoparticle with a diameter of 0.21 nm over 1 ns. (b) Three-dimensional Cartesian coordinate frames defined for the pyramid-shaped nanoparticle where the *z*-axis is along its initial orientation (from the center of the bottom face to the top atom) and the origin at its center of mass and for the spherical nanoparticle where the *z*-axis is along the initial vector pointing from its center of mass to one atom on the surface. The left and right images on each row show the side and bottom views of each nanoparticle, respectively. Both frames are defined at initial time and fixed thereafter for data analysis. (c) Ensemble-averaged trajectories (solid curves) of the pyramid-shaped nanoparticle in the *x*-*z* plane for different directions of the initial velocity as displayed in different colors. The dashed circles and lines are included as visual guides. (d) Sampled 50-ps trajectories of the nanoparticle starting from different initial orientations (*z*-axes). (e) Ensemble-averaged trajectories and (f) mean velocities of the two nanoparticles in the cases where their initial velocities are in the direction along the *x*-axis that is perpendicular to the initial orientations (*z*-axis), together with the simulation results for the self-propelled spherical nanoparticle as an active nanoparticle for comparison. The open circles in (e) indicate the points where the mean center of mass positions of the nanoparticles cease to move after about 10 ps.

2 Results from MD simulations

The simulation system consisted of a single model nanoparticle shaped as a triangular pyramid immersed in a solvent of small Lennard–Jones (LJ) particles with periodic boundary conditions applied in all three directions, as described in the Simulation Method. Each MD simulation was first run for 20 ns to equilibrate the system and then for another 200 ns for data analysis. From five independent simulation runs, we collect abundant samples of the nanoparticle trajectories with the same time interval of 50 ps. As illustrated in Fig. 1(b) and (d), a three-dimensional (3D) Cartesian coordinate frame was defined for every sampled trajectory of the particle with the *z*-axis along its initial orientation (from the center of the bottom face to the top atom) and the origin at its center of mass (CoM). For comparison, we also simulated another system where the

asymmetrically shaped nanoparticle was replaced by a spherical nanoparticle with the same mass, atom number, and volume, whose orientation was defined by the vector pointing from its CoM to an atom on the surface.

Fig. 1(a) shows the typical trajectories of the pyramid-shaped and spherical nanoparticles over 1 ns, demonstrating the homologous random feature of particle movement under thermal fluctuations. It is clear that the ensemble-averaged trajectory better reflects the intrinsic feature of the motion from noise. As presented in Fig. 1(e), just as one would generally expect without taking into account the shapes of molecules/particles, the averaged trajectory of the spherical nanoparticle follows a straight line along the direction of its initial velocity because of inertia. As its inertia decays owing to the collisions with the surrounding solvent, the averaged trajectory of the spherical nanoparticle finally ends at a point. We note that the end point of the trajectory does not mean that the nanoparticle is motionless; instead, it corresponds to an almost-zero ensemble-averaged velocity caused by the isotropic probability of the motion. The pyramid-shaped nanoparticle initially shows similar inertial motion. Surprisingly, as time passes, the ensemble-averaged trajectory of the asymmetric nanoparticle spontaneously curves toward the direction of its original orientation (positive z-direction), even though the initial velocity was in a perpendicular direction (positive x-direction). It is also interesting to note that in contrast to the monotonic decrease of the mean velocity $<v_x(t)>$ of the asymmetrically shaped nanoparticle along its initial velocity direction (x-direction), its mean velocity along the z-direction $<v_z(t)>$ increases from zero to a peak value at t = 1.08 ps and then gradually decreases to zero [Fig. 1(f)]. Accordingly, the mean CoM position of this nanoparticle drifts away from the origin and finally settles at a point with coordinates x = 0.10 nm and z = 0.04 nm after about 10 ps. Thus, the motion of the asymmetrically shaped nanoparticle consists of two parts; i.e., the expected inertial motion along the initial velocity direction (the x-direction here) and the unexpected directional motion towards the initial orientation direction (the z-direction here). To provide a complete picture, Fig. 1(c) shows the ensemble-averaged trajectories of the asymmetrically shaped nanoparticle starting with initial velocities in all different directions (not only the x-direction as discussed above) with respect to the initial orientation (positive z-direction). Clearly, all of these trajectories display the bending curvature towards the z-direction.

Now we focus on understanding the physical origin of this spontaneously curved trajectory of the asymmetrically shaped nanoparticle by analyzing the ensemble-averaged force $<F_z^i(t)>$ acting on every individual constituent atom, where i is the serial number of the atom under investigation. Apparently, $<F_z^i(t)>$ results from the fluctuating forces caused by collisions with surrounding solvent molecules and the internal force originating from the bonds with the other constituent atoms. Following the Stokes law, this force is considered to be linearly proportional to the mean velocity of the ith atom along the z-direction $<v_z^i(t)>$,

$$\left\langle F_z^i(t)\right\rangle = -\lambda^i \left\langle v_z^i(t)\right\rangle, \qquad (1)$$

where λ^i is the frictional coefficient of atom i. We note that the value of λ^i varies for atoms located at different sites in the particle structure, depending on how they are in contact with the solvent. In practice, the frictional coefficient of each atom can be estimated from the linear relation between $<F_z^i(t)>$ and $<v_z^i(t)>$ (details are provided in Appendix A1).

In addition, $<v_z^i(t)>$ can be written as

$$\left\langle v_z^i(t)\right\rangle = \left\langle v_z(t)\right\rangle - r_o^i(t)Q(t), \text{where } Q(t) = -\frac{d}{dt}C_\varphi(t), \quad (2)$$

because the motion of each constituent atom could be separated into the CoM motion of the nanoparticle, denoted by $<v_z(t)>$ in Eq. (2), plus the rotation around the CoM denoted by the second term on the right-hand side (rhs) of Eq. (2). r_o^i is the projection of the atom position vector $\mathbf{r}^i$ pointing from the particle CoM to the ith atom on the particle orientation axis (unit vector denoted by $\mathbf{i}$), i.e., $r_o^i = \mathbf{r}^i \cdot \mathbf{i}$, and can be obtained directly from the nanoparticle structure (details are provided in Appendix A2). The differential $Q(t)$ of the particle orientation autocorrelation function $C_\varphi(t) = <\mathbf{i}(0)\cdot\mathbf{i}(t)> = <\cos[\varphi(t)]>$ characterizes the particle rotational relaxation, where $\varphi(t)$ is the particle orientation angle with respect to its original orientation. Suppose that the asymmetrically shaped particle rotates around its CoM with an angular velocity $\boldsymbol{\omega}$. As sketched in Fig. 2(a) for two typical constituent atoms, the velocity of atom i has a rotation-related component of the form $\boldsymbol{\omega}\times\mathbf{r}^i$. When moving with this velocity, the atom experiences an effective frictional force arising from collisions with surrounding molecules $-\lambda^i(\boldsymbol{\omega}\times\mathbf{r}^i)$. Fig. 2(a) demonstrates that these effective forces differ for atoms located at different sites, which results in a non-zero net force at the CoM of the nanoparticle and consequently affects its movement. After taking the ensemble average, the mean projection of the velocity of atom i on the initial orientation $\mathbf{i}(0)$ is $<[\boldsymbol{\omega}(t)\times\mathbf{r}^i(t)]\cdot\mathbf{i}(0)> = -<[\mathbf{i}(0)\times\mathbf{r}^i(t)]\cdot\boldsymbol{\omega}(t)> = -r_o^i<[\mathbf{i}(0)\times\mathbf{i}(t)]\cdot\boldsymbol{\omega}(t)> = -r_o^iQ(t)$ and the mean effective frictional force is $\lambda^i r_o^i Q(t)$. We substituted Eq. (2) into Eq. (1) and added up all the effective frictional forces acting on the constituent atoms of the asymmetrically shaped nanoparticle to get

$$\left\langle F_z(t)\right\rangle = \sum_{i=1}^{N}\left\langle F_z^i(t)\right\rangle = -mC_1\left\langle v_z(t)\right\rangle + mC_2Q(t) \qquad (3)$$

with

$$C_1 = \frac{\sum_{i=1}^{N}\lambda^i}{m}, \quad C_2 = \frac{\sum_{i=1}^{N}\lambda^i r_o^i}{m}, \qquad (4)$$

where m is the total mass of the nanoparticle. The first term on the rhs of Eq. (3) always resists the translational motion of the particle. It is the second term that could potentially provide an effective force to generate the mean displacement of the particle CoM along the z-direction. We calculated C_1 and C_2 directly based on Eq. (4) and obtained values of 2.79 and 0.11 nm ps^{-1}, respectively (calculation details are in Appendix A1). By solving Newton's second law, which is a differential equation of velocity, we obtained $\langle v_z(t)\rangle$,

$$\left\langle v_z(t)\right\rangle = C_2R(t) \quad \text{with} \quad R(t) = e^{-C_1t}\int_0^t Q(\xi)e^{C_1\xi}d\xi\,. \qquad (5)$$

We also computed $C_\varphi(t)$ of the nanoparticle orientation from the MD trajectories. In classical rotational Brownian motion, $C_\varphi(t)$ is predicted to decay exponentially over time [18]. However, our simulation data in Fig. 2(b) show that in the very first picosecond where the inertial effect dominates, $C_\varphi(t)$ does not follow an exponential form. A standard biexponential function of the form

$$C_\varphi(t) = \frac{\tau_1}{\tau_1-\tau_2}e^{-t/\tau_1} - \frac{\tau_2}{\tau_1-\tau_2}e^{-t/\tau_2}, \qquad (6)$$

with the characteristic times τ_1 = 1.82 ps and τ_2 = 0.25 ps was found to describe the data very well.

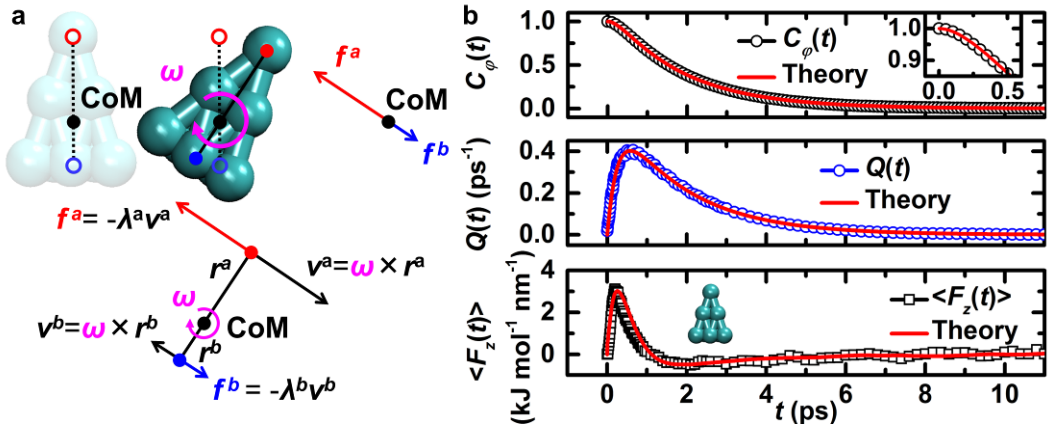

Figure 2 (a) Sketch of the rotation-related velocities of one top and one bottom atom of the pyramid-shaped nanoparticle and the effective frictional forces acting on them by surrounding solvent molecules. The contributions of these forces to the translational motion of the particle via its center of mass are shown in the lower part of this panel. (b) Autocorrelation function of the particle orientation $C_\varphi(t)$ (black circles), its rate of variation $Q(t)$ (blue circles), and the mean force experienced by the center of mass of the nanoparticle along the z-axis (black squares). The inset is an enlarged image of $C_\varphi(t)$ in the first 0.5 ps. The red curves are theoretical predictions of Eq. (6) (upper), its derivative (middle), and Eq. (7) (lower).

The mean force acting on the CoM of the nanoparticle was thus obtained by substituting Eq. (5) and (6) into Eq. (3)

$$\left\langle F_z(t)\right\rangle = mC_2\left[Q(t) - C_1R(t)\right], \qquad (7)$$

which provided a good description of the simulation results, as shown in Fig. 2(b). It is clear that $\langle F_z(t)\rangle$ does have a positive value towards the initial orientation **i**(0) of the particle after a short time. More specifically, this force first increases from zero, reaches its maximal value at about 0.2 ps, and then decreases. $\langle F_z(t)\rangle$ becomes negative at 1 ps, reaches its minimal value at about 2 ps, and then gradually approaches zero. Eq. (7) further clarifies that the mean force on the nanoparticle can be non-zero only when $C_2 \neq 0$ and $[Q(t) - C_1R(t)] \neq 0$. The contribution of the asymmetric architecture of the nanoparticle is carried by C_2 because it possesses the position vector of every atom. The terms in the square brackets are all related to rotational motion. This indicates that the key reason for the non-zero net force $\langle F_z(t)\rangle$ lies in the imbalance of the effective frictional forces or hydrodynamic resistance ($C_2 \neq 0$) acting on the constituent atoms during the regulation of particle orientation. This can only happen for particles with asymmetric structures. If the geometric shape of the particle is symmetric, the effective frictional forces acting on all atoms are well balanced ($C_2 = 0$) and no directional motion can be observed (see the example in Appendix A3). Meanwhile, the rotational motion of the nanoparticle also plays an important role in its behavior. If we fix the orientation of the particle [$C_\varphi(t) = 1$], $Q(t)$ and $R(t)$ in Eq. (7) both equal zero. Then, even for an

asymmetrically shaped nanoparticle with $C_2 \neq 0$, the mean force is zero. Therefore, the key of nonzero mean force is asymmetry, meanwhile, the rotation is also required.

Based on the theoretical analyses above, we imposed an additional force of $\mathbf{F}_{add}(t) = 340[\mathbf{i}(t)\times\mathbf{L}(t)]$ pN on the CoM of a spherical nanoparticle, where $\mathbf{i}(t)$ is the unit vector pointing from the particle CoM to a certain atom on the surface and $\mathbf{L}(t)$ is the angular momentum of the rotation. This self-propelled active nanoparticle is found to possess a very similar curved mean trajectory to that of the pyramid-shaped nanoparticle. As illustrated in Fig. 1(e), the mean particle trajectory also bends towards the direction of its original orientation $\mathbf{i}$ (positive z-direction), even though the initial velocity was in a perpendicular direction (positive x-direction). The particle settles at a final position with coordinates $x = 0.10$ nm and $z = 0.05$ nm. The average velocity of the self-propelled particle along the z-direction rises from zero to the peak at $t = 0.71$ ps and then decreases to zero. There is a small bulge in the velocity at $t = 2.33$ ps, which causes a small wave near the tail of the trajectory. This might be caused by some hidden influence of the additional force during the rotational relaxation. The similarity of the curved trajectories of the self-propelled spherical nanoparticle and freely moving pyramid-shaped nanoparticle suggests that the asymmetrically shaped nanoparticle bears a certain amount of activity analogous to that of self-propelled active matter.

3 Conclusion and Discussion

To summarize, we have shown by molecular dynamics simulations that the motion of an asymmetrically shaped nanoparticle with broken central symmetry in dilute solution possesses a spontaneously curved trajectory within a finite time interval, instead of the generally expected random walk. This unexpected dynamic behavior has a similarity to that of active matters [48–51]. However, different from self-propelled active matter, which consumes energy to provide a driving force [51–54], here the non-zero resultant force solely results from thermal fluctuations. We have also derived theoretical formulae that can well describe the physical origin of this non-zero resultant force.

We note that the hydrodynamic theory of Brownian motion in fluids at small Reynolds number has been extended to particles with irregular shapes in the series of classic papers by Brenner [55-57]. And the translation-rotation coupled tensor successfully describes the anisotropic diffusion of asymmetric colloidal particles observed in experiments [19,58]. However, at the molecular scale, the translation-rotation coupled motion arises within the relaxation of momentum, which may carry out in very finite time before the diffusion regime. Therefore, we demonstrate our data from the simulations by using force analysis rather than the hydrodynamic theory.

A further remark we would like to make is that the observed curvature in the trajectory of the particle will not lead to a perpetuum mobile that violates the second law of thermodynamics. As shown above, the trajectory spontaneously bends towards the direction along the initial orientation of the shaped particle. In equilibrium systems with sufficiently long time or a sufficiently large number of particles for averaging, the orientations of the nanoparticles will have equal probability in all directions. After averaging over all possible initial orientations of the particles, the mean displacement is zero, so there is no directional flow in the system. This is consistent with statistical mechanics principles. In Appendix A4, we have demonstrated that one cannot extract mechanical energy from a thermal bath by restraining the orientations of the particles. However, for the case where we only focus on the motion of a single molecule within a finite time, we will observe a directional curved trajectory and spontaneous active motion.

Considering that a majority of physical, chemical and biological processes happen on the nanoscale within finite timescales and most of the involved molecules possess asymmetric structures, we expect that a directional curved trajectory may have significant influence on various processes such as nucleation of clusters, self-assembly, chemical reaction initiation, intercellular signal transduction, and neurotransmission. For example, intracellular signaling is usually carried out by small signal molecules over a distance of several nanometers to their receptors on a finite timescale [32–34]. However, how to evaluate the role of the directional curved trajectory in the dynamics of these processes remains to be an open and challenging research subject.

4 Simulation method

The model nanoparticle we simulated was shaped as a triangular pyramid with height $h = 0.37$ nm, as shown in Fig. 1(a). The

three side surfaces of the particle are identical isosceles triangles with an angle of 36° and the bottom surface is regular triangles. The asymmetrically shaped nanoparticle was constructed by bonding ten LJ particles. We put the model nanoparticle in a cubic box with dimensions of 4 nm × 4 nm × 4 nm with periodic boundary conditions filled with 1086 LJ particles as solvent. As detailed in Appendix A5, the size of the simulation box is large enough and then the finite size effect is negligible. All LJ particles had the same mass of m_{LJ}=12.011 u and the same force-field parameters (σ = 0.375 nm, ε = 0.439 kJ mol^{-1}). For comparison, a spherical nanoparticle in an individual system was constructed with the same atom number, mass, and volume, approximating a sphere with a diameter of about 0.20 nm. In another system, a self-propelled spherical nanoparticle had an additional force of 340(**i**×**L**) pN imposed on its CoM, where **i** is the unit vector pointing from the particle CoM to a certain atom on the surface and **L** is the angular momentum of the rotation in unit of u nm^2 ps^{-1}. The cut-off distance for van de Waals interactions was set to 1.3 nm. There was no Coulomb interaction in this system. The temperature was maintained at 300 K by a velocity-rescale thermostat [59]. A time step of 2 fs was used, and the neighbor list was updated every ten steps. Using Gromacs 4.6 software [60], we performed five independent simulation runs for each system containing a single model particle immersed in solvent, starting from different initial configurations. Each system was first equilibrated for 20 ns and then run for another 200 ns for analysis. The statistical calculations were carried out by taking time origins separated by 1 ps along the MD trajectory. Thus, we had about one million samples of each model nanoparticle for statistical analysis.

We thank Prof. Qing JI and Prof. Jun HU for helpful discussions. Z. Wang also acknowledges Alexei Likhtman, Alex Lukyanov, and Eugene Terentjev for valuable discussions. This work was supported by the National Natural Science Foundation of China (Grant Nos. 10825520, 11422542, 11175230, and 11290164), the Key Research Program of the Chinese Academy of Sciences (Grant No. KJZD-EW-M03), Deepcomp7000 and ScGrid of the Supercomputing Center, the Computer Network Information Center of the Chinese Academy of Sciences, and the Shanghai Supercomputer Center of China.

1 P. Kral, L. Vukovic, N. Patra, B. Wang, K. Sint, and A. Titov, J. Nanosci. Lett. **1**, 128 (2012).
2 J. H. Bahng, B. Yeom, Y. Wang, S. O. Tung, J. D. Hoff, and N. Kotov, Nature **517**, 596 (2015).
3 L. Zhao, C. Wang, J. Liu, B. Wen, Y. Tu, Z. Wang, and H. Fang, Phys. Rev. Lett. **112**, 78301 (2014).
4 D. Chandler, Nature **437**, 640 (2005).
5 P. Hervés, M. Pérez-Lorenzo, L. M. Liz-Marzán, J. Dzubiella, Y. Lu, and M. Ballauff, Chem. Soc. Rev. **41**, 5577 (2012).
6 J. Yang, G. Shi, Y. Tu, and H. Fang, Angew. Chemie Int. Ed. **53**, 10190 (2014).
7 B. Song, Q. Sun, H. Li, B. Ge, J. S. Pan, A. T. S. Wee, Y. Zhang, S. Huang, R. Zhou, X. Gao, F. Huang, and H. Fang, Angew. Chemie Int. Ed. **53**, 6358 (2014).
8 P. Ball, Chem. Rev. **108**, 74 (2008).
9 R. Philips, J. Kondev, and J. Theriot, *Physical Biology of the Cell* (Garland Science, 2008).
10 B. L. de Groot and H. Grubmüller, Science **294**, 2353 (2001).
11 Y. von Hansen, S. Gekle, and R. R. Netz, Phys. Rev. Lett. **111**, 118103 (2013).
12 C. Di Rienzo, V. Piazza, E. Gratton, F. Beltram, and F. Cardarelli, Nat. Commun. **5**, 1 (2014).
13 R. M. Robertson, S. Laib, and D. E. Smith, Proc. Natl. Acad. Sci. U. S. A. **103**, 7310 (2006).
14 I. Echeverria, D. E. Makarov, and G. A. Papoian, J. Am. Chem. Soc. **136**, 8708 (2014).
15 A. Einstein, Ann. Phys. **322**, 549 (1905).
16 A. Einstein, Zeitschrift Für Elektrotechnik Und Elektrochemie **13**, 41 (1907).
17 D. Chandler, *Introduction to Modern Statistical Mechanics* (Oxford University Press, 1987).
18 M. Doi and S. F. Edwards, *The Theory of Polymer Dynamics* (Clarendon Press, 1988).
19 Y. Han, A. M. Alsayed, M. Nobili, J. Zhang, T. C. Lubensky, and A. G. Yodh, Science **314**, 626 (2006).
20 T. Li and M. G. Raizen, Ann. Phys. **525**, 281 (2013).
21 R. Huang, I. Chavez, K. M. Taute, B. Lukić, S. Jeney, M. G. Raizen, and E.-L. Florin, Nat. Phys. **7**, 576 (2011).
22 A. Schlaich, E. W. Knapp, and R. R. Netz, Phys. Rev. Lett. **117**, 48001 (2016).
23 H. Qiu, X. C. Zeng, and W. Guo, ACS Nano **9**, 9877 (2015).
24 L. Ma, A. Gaisinskaya-Kipnis, N. Kampf, and J. Klein, Nat. Commun. **6**, 6060 (2015).
25 A. Barati Farimani, N. R. Aluru, and E. Tajkhorshid, Appl. Phys. Lett. **105**, 83702 (2014).
26 T. Franosch, M. Grimm, M. Belushkin, F. M. Mor, G. Foffi, L. Forró, and S. Jeney, Nature **478**, 85 (2011).
27 P. N. Pusey, Science **332**, 802 (2011).
28 N. Arai, K. Yasuoka, and X. C. Zeng, J. Am. Chem. Soc. **130**, 7916 (2008).
29 A. Reinhardt and D. Frenkel, Soft Matter **12**, 6253 (2016).
30 X. Zhou, G. Liu, K. Yamato, Y. Shen, R. Cheng, X. Wei, W. Bai, Y. Gao, H. Li, Y. Liu, F. Liu, D. M. Czajkowsky, J. Wang, M. J. Dabney, Z. Cai, J. Hu, F. V. Bright, L. He, X. C. Zeng, Z. Shao, and B. Gong, Nat. Commun. **3**, 949 (2012).
31 T. Guérin, O. Bénichou, and R. Voituriez, Nat. Chem. **4**, 568 (2012).
32 M. J. Berridge and R. F. Irvine, Nature **341**, 197 (1989).
33 M. Rodbell, Nature **284**, 17 (1980).
34 N. A. Campbell and J. B. Reece, *Biology* (Benjamin Cummings, 2002).
35 B. Barbour and M. Häusser, Trends Neurosci. **20**, 377 (1997).
36 R. Wan, C. Wang, X. Lei, G. Zhou, and H. Fang, Phys. Rev. Lett. **115**, 195901 (2015).
37 P. Guo, Y. Tu, J. Yang, C. Wang, N. Sheng, and H. Fang, Phys. Rev. Lett. **115**, 186101 (2015).
38 Y. Huang, C. Zhu, L. Wang, X. Cao, Y. Su, X. Jiang, S. Meng, J. Zhao, and X. C. Zeng, Sci. Adv. **2**, e1501010 (2016).
39 G. Hummer, J. C. Rasaiah, and J. P. Noworyta, Nature **414**, 188 (2001).

40 J. Yang, S. Meng, L. F. Xu, and E. G. Wang, Phys. Rev. Lett. **92**, 146102 (2004).
41 B. Wang and P. Král, Phys. Rev. Lett. **101**, 46103 (2008).
42 I. Kosztin and K. Schulten, Phys. Rev. Lett. **93**, 238102 (2004).
43 C. Zhu, H. Li, Y. Huang, X. C. Zeng, and S. Meng, Phys. Rev. Lett. **110**, 126101 (2013).
44 R. Zhou, X. Huang, C. J. Margulis, and B. J. Berne, Science **305**, 1605 (2004).
45 Q. Zhang, W. Jiang, J. Liu, R. Miao, and N. Sheng, Phys. Rev. Lett. **110**, 254501 (2013).
46 N. Sheng, Y. S. Tu, P. Guo, R. Z. Wan, and H. P. Fang, J. Hydrodyn. Ser. B **24**, 969 (2012).
47 N. Sheng, Y. S. Tu, P. Guo, R. Z. Wan, and H. P. Fang, Sci. China Physics, Mech. Astron. **56**, 1047 (2013).
48 M. C. Marchetti, J. F. Joanny, S. Ramaswamy, T. B. Liverpool, J. Prost, M. Rao, and R. A. Simha, Rev. Mod. Phys. **85**, 1143 (2013).
49 C. Krüger, G. Klös, C. Bahr, and C. C. Maass, Phys. Rev. Lett. **117**, 48003 (2016).
50 P. K. Ghosh, Y. Li, G. Marchegiani, and F. Marchesoni, J. Chem. Phys. **143**, 211101 (2015).
51 É. Fodor, C. Nardini, M. E. Cates, J. Tailleur, P. Visco, and F. van Wijland, Phys. Rev. Lett. **117**, 38103 (2016).
52 P. Romanczuk and L. Schimansky-Geier, Phys. Rev. Lett. **106**, 230601 (2011).
53 I. Buttinoni, G. Volpe, F. Kümmel, G. Volpe, and C. Bechinger, J. Phys. Condens. Matter **24**, 284129 (2012).
54 H. Wioland, F. G. Woodhouse, J. Dunkel, and R. E. Goldstein, Nat. Phys. **12**, 1 (2016).
55 H. Brenner, Chem. Eng. Sci. **18**, 1 (1963).
56 H. Brenner and R. G. Cox, J. Fluid Mech. **17**, 561 (1963).
57 H. Brenner, J. Colloid Sci. **20**, 104 (1965).
58 A. Chakrabarty, A. Konya, F. Wang, J. V. Selinger, K. Sun, Q.-H. Wei, and A. Arbor, Phys. Rev. Lett. **111**, 160603 (2013).
59 G. Bussi, D. Donadio, and M. Parrinello, J. Chem. Phys. **126**, 14101 (2007).
60 B. Hess, C. Kutzner, D. van der Spoel, and E. Lindahl, J. Chem. Theory Comput. **4**, 435 (2008).
61 I. Yeh and G. Hummer, J. Phys. Chem. B **108**, 15873 (2004).

Appendix A1 Frictional coefficients of constituent atoms of the model particles

Fig. A1.1(a) shows the structure of the pyramid-shaped nanoparticle we studied in the main text with h = 0.37 nm composed of ten atoms. The atoms are divided into four types according to the trigonal symmetry of the particle. Fig. A1.1(b) presents the ensemble-averaged velocity $\langle v_z^i(t)\rangle$ and ensemble-averaged force $\langle F_z^i(t)\rangle$ for each type of atom. $\langle F_z^i(t)\rangle$ acting on each individual constituent atom of the particle results from the fluctuating forces arising from collisions with surrounding solvent molecules and the internal force originating from the bonds with the other constituent atoms. The data suggest that there is a linear relation between the mean force and mean velocity of each atom, $\langle F_z^i(t)\rangle = -\lambda^i\langle v_z^i(t)\rangle$, which consequently gives the frictional coefficient λ^i of each atom (Table A1.1).

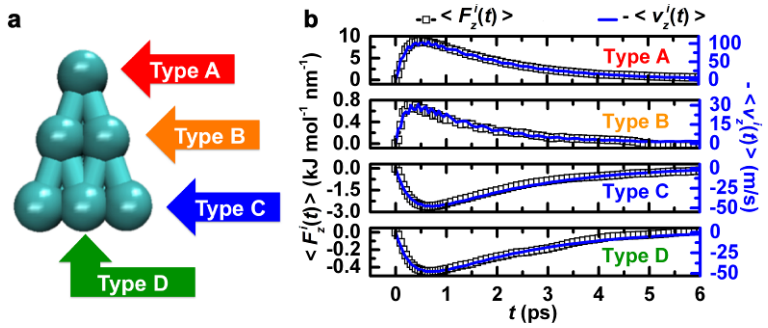

Figure A1.1 (a) Structure of the asymmetric particle. The atoms are divided into four types according to their geometric locations in the particle. (b) Mean force and mean velocity of each type of atom in the asymmetric particle with respect to time.

Table A1.1 Frictional coefficient and the projection of the position vector, which points from the center of mass of the particle to an atom of each type, on the particle orientation axis.

Type	Type A	Type B	Type C	Type D
λ^i (kJ mol^{-1} nm^{-2} ps)	85.05	23.14	51.72	8.64
r_o^i (nm)	0.28	0.09	-0.09	-0.09

When we sum up all the mean forces on each constituent atom, it is notable that there exists a non-zero net force $\langle F_z(t)\rangle$ on the particle along the z-axis within a finite timescale. Accordingly, this non-zero net force along the z-axis causes non-zero mean velocity of the nanoparticle along the z-axis [Fig. 1(d) in the main text] and a directional drift of the mean position $\langle z(t)\rangle$ of the asymmetrically shaped nanoparticle, which is obtained by integrating the mean velocity,

$$\langle z(t)\rangle = \int_0^t \langle v_z(\xi)\rangle d\xi = \frac{C_2}{C_1}\left[1 - C_\varphi(t) - R(t)\right]. \quad \text{(A1.1)}$$

The simulation results in Fig. A1.2 are well described by Eq. (7) in the main text and Eq. (A1.1) using the values of $C_1 = 2.79$ ps^{-1} and $C_2 = 0.11$ nm ps^{-1} as directly calculated from Table A1.1.

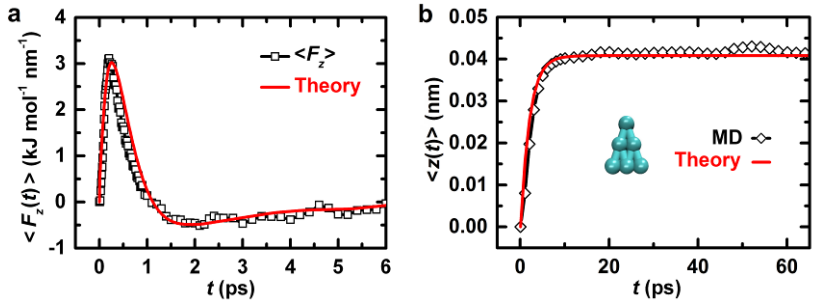

Figure A1.2 (a) Net force on the nanoparticle (black open squares) with respect to time obtained directly from MD simulations. The solid red curve is the theoretical prediction based on Eq. (5) using C_1 and C_2 values calculated from Table A1.1. (b) Mean displacement of the nanoparticle (black open squares) with respect to time obtained directly from MD simulations. The solid red curve is the theoretical prediction based on Eq. (A1.1) using C_1 and C_2 values calculated from Table A1.1.

Appendix A2 Projection of an atom position vector on the particle orientation direction

Because the particle can rotate around its orientation axis, the position vector pointing from the CoM of the particle to that of a constituent atom may change in different samples even though the orientation of the particle in these samples remains the same. We should perform an ensemble average for the cases with the same φ in which the particle rotates around its orientation axis in a three-dimensional system. Fig. A2.1(a) is a sketch of the system where O is the CoM of the particle and A is the position of the atom in a randomly selected sample. $\overrightarrow{OA}$ is the position vector from the particle CoM to the atom in this sample. $\overrightarrow{OC}$ is the projection of $\overrightarrow{OA}$ on the orientation of the particle. Because the atom can rotate around the orientation axis, there must exist samples in which the position of the atom is at another point B, which is located on the circle and is to the other end of the diameter vector $\overrightarrow{ACB}$, where C is the center of the circle. Then, we projected the position vectors on the **z**-axis and obtained $\overrightarrow{OA'}$ and $\overrightarrow{OB'}$ (Fig. A3.1(b)). We note that $\overrightarrow{OA'} \neq \overrightarrow{OB'}$. We also projected $\overrightarrow{OC}$ on the z-axis to obtain $\overrightarrow{OC'}$.

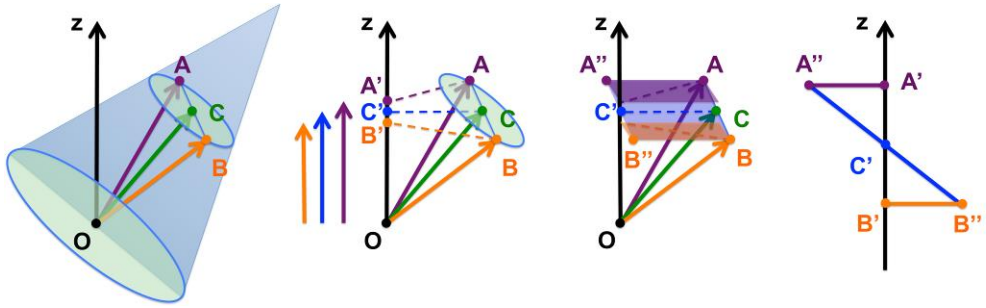

Figure A2.1 Sketches of the projection of atom position vectors on the orientation axis of a particle and on the original orientation direction (z-axis) for averaging over samples in which the particle rotates around its orientation axis. O is the center of mass of the particle. The black arrow is the z-axis. $\overrightarrow{OA}$ is the vector in a randomly selected sample. $\overrightarrow{OC}$ is the projection of $\overrightarrow{OA}$ on the orientation axis (green arrow). $\overrightarrow{OB}$ is the position vector of the same atom in another sample and $\overrightarrow{ACB}$ is the diameter of the rotation circle. A', B' and C' are the projections of A, B and C, on the z-axis, respectively. A'' and B'' are the translational locations of points A and B along the vector $\overrightarrow{CC'}$.

If we translate A and B to A'' and B'' along the vector $\overrightarrow{CC'}$, then the surface S ($AA'A''$) is vertical to the z-axis, which implies $\overrightarrow{A'A''} \perp \mathbf{z}$. Similarly, we obtain $\overrightarrow{B'B''} \perp \mathbf{z}$. Because the lengths of $\overrightarrow{CA}$ and $\overrightarrow{CB}$ are equal, the length of $\overrightarrow{C'A''}$ equals that of $\overrightarrow{C'B''}$. Then, the triangles $\Delta AA''C'$ and $\Delta BB''C'$ are congruent triangles, which implies $\left|\overrightarrow{C'A'}\right| = \left|\overrightarrow{C'B'}\right|$ and C' is the midpoint of $\overrightarrow{A'B'}$. Thus,

$$\overrightarrow{OC'} = \frac{\overrightarrow{OA'} + \overrightarrow{OB'}}{2}. \tag{A2.1}$$

The above geometric discussion suggests that the sample average of the projection of the position vector $\mathbf{r}^i$ onto the z-axis can be obtained by dividing the calculation into two steps. We first project the position vector $\mathbf{r}^i$ to the orientation axis for averaging over samples where the particle rotates around the orientation axis to obtain r_o^i ($\overrightarrow{OC}$ in the above notation). Then, we project the vector $r_o^i\mathbf{i}(t)$ onto the z-axis by multiplying r_o^i with the autocorrelation function of the particle orientation $C_\varphi(t)$,

$$r_o^i \left\langle \mathbf{i}(t)\cdot\mathbf{i}(0)\right\rangle = r_o^i \left\langle \cos\varphi\right\rangle = r_o^i C_\varphi(t). \tag{A2.2}$$

Because the velocity is the first-order derivative of the atom position, the rotation-related component of the atom velocity is associated with $C_\varphi(t)$ as

$$\frac{d}{dt}\left[r_o^i C_\varphi(t)\right] = r_o^i \frac{d}{dt} C_\varphi(t). \tag{A2.3}$$

Appendix A3 Analysis of a symmetric nanoparticle

We also investigated the motion of a symmetric nanoparticle for comparison. The structure of a rod-like symmetric nanoparticle with h = 0.3 nm is shown in Fig. A3.1(a), where the four constituent atoms of the nanoparticle are named individually. We note that the ensemble-averaged velocities and ensemble-averaged forces of the four atoms show symmetric behavior [Fig. A3.1(b, c)]. The positive and negative mean forces are well balanced with each other, and the net force acting on the symmetric particle along the original particle orientation direction is almost zero with some fluctuations [Fig. A3.1(d)].

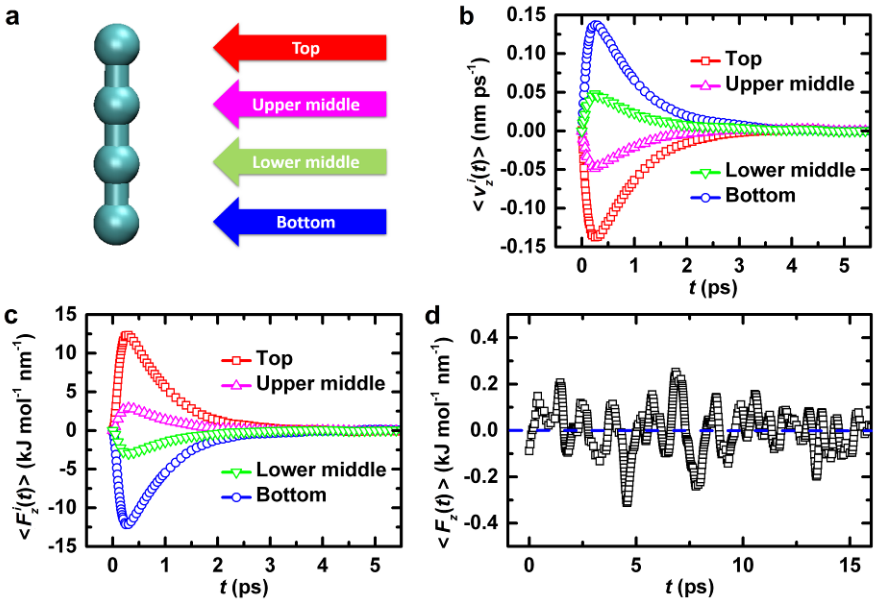

Figure A3.1 (a) Structure of the rod-like symmetric particle. The four atoms are named individually. (b) Mean velocity and (c) mean force of each atom along the z-direction. (d) Net force acing on the rod-like symmetric nanoparticle along the z-direction.

Table A3.1 Frictional coefficient and the projection on the particle orientation axis of the position vector pointing from the center of mass of the particle to an atom of each type.

Type	Top	Upper middle	Lower middle	Bottom
λ^i (kJ mol^{-1} nm^{-2} ps)	89.43	64.57	64.57	89.43
r_o^i (nm)	0.2	0.1	-0.1	-0.2

Appendix A4 Can directional drift lead to a perpetuum mobile?

As discussed in the main text, the directional drift behavior of asymmetric model particles only takes place along their initial orientation. In equilibrium systems, the orientations of the particles have equal probability in all directions. After averaging over all possible initial orientations of the particles, the mean displacement of the particles is zero at any time and so there is

no directional drift, which is consistent with the equilibrium statistical mechanics. Thus, we will not obtain a perpetuum mobile.

The drift behavior of asymmetric particles is a physical result of the translation–rotation coupling. To further elucidate this, we refer to Eq. (A1.1) above (repeated here),

$$\langle z(t)\rangle = \int_0^t \langle v_z(\xi)\rangle d\xi = \frac{C_2}{C_1}\left[1 - C_\varphi(t) - R(t)\right]. \qquad \text{(A1.1)}$$

This equation implies that if we fix the orientation of the particle [$C_\varphi(t) = 1$, $R(t) = 0$], the drift will vanish [$\langle z(t)\rangle = 0$]. We carried out further MD simulations to verify this coupling effect. In these additional simulations, we applied a pair of forces on the top and bottom atoms of the model particle, respectively, to restrain its orientation. The forces have the same magnitude but opposite directions. Such restriction of the particle rotation can also be understood as mimicking the action of an external field on a dipole moment embedded in the model particle. Figure A4.1 shows the results for different magnitudes for this orientation restraint. The strength of the applied restraint forces was 0.3 kJ mol^{-1} nm^{-1} to represent weak restraint, and 0.6 kJ mol^{-1} nm^{-1} in the case of strong restraint. Fig. A4.1(a) reveals that the orientation correlation function $C_\varphi(t)$ is obviously affected by orientation restraint as the strength of the restraint force increases. As predicted by Eq. (A1.1), the magnitude drift decreases strongly as the orientation restraint becomes stronger. Therefore, one cannot achieve directional drift by simply fixing the orientation of the particle. Furthermore, considering that the directional drift only takes place over a timescale comparable to the characteristic rotational relaxation time of the particle and saturates at a magnitude that is only a fraction of the particle size, there is no way to extract mechanical energy from a thermal bath without violating the thermodynamics laws.

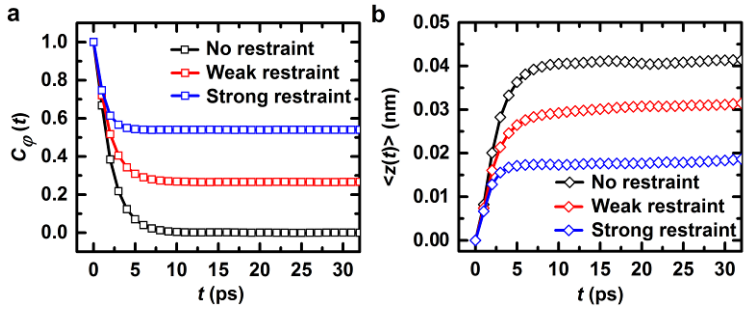

Figure A4.1 (a) Autocorrelation functions of orientation $C_\varphi(t)$ and (b) mean displacements $\langle z(t)\rangle$ along the z-axis of the model particles under orientation-restraint forces of different strength.

As we stated in the conclusions section in the main text, to make use of this drift behavior, one either needs to control the initial orientations of the particles, which requires energy input, or to be able to track the instantaneous orientation of the particle by advanced experimental techniques.

Appendix A5 Examining possible finite size effects

To examine the influence of possible finite size effects on our simulation results, we performed three extra MD simulation runs to study the Brownian motion of a pyramid-shaped nanoparticle with $h = 0.37$ nm in dilute solutions. The side length of the cubic simulation box is consecutively increased by a factor of two from $L_{\text{Box}} = 4$ nm to 8 nm and then to 16 nm. As shown in Fig A5.1(a), the simulation results for the time-dependent mean displacement $\langle z(t)\rangle$ of the model nanoparticle obtained from the three different systems agree with each other very well. This indicates that the size of our simulation box (see Simulation Method in the main text) is large enough to make the influence of finite size effects on the directional motion behavior of the model particles nearly negligible.

In contrast, the simulation results for the velocity autocorrelation function (VACF) do show a sign of system size-dependent behavior. Fig. A5.1(b) reveals that the three VACF curves initially agree with each other very well. They decay quickly over time to values less than 1% at $t \approx 4$ ps, and then start to show large timescale fluctuations and also deviate from each other. These fluctuation tails could be attributed to the hydrodynamic correlations between neighboring boxes. In simulations, it is difficult to extract the periodicity of these fluctuations from the VACFs of the single model particle. Instead, we look at the time when the VACF first decays below zero, which represents a negative correlation of velocity. The inset in Fig. A5.1(b)

reveals that this time is about 9 ps for the smallest box (L_{Box} = 4 nm) and about 17 ps when the box size is doubled (L_{Box} = 8 nm). The VACF for the system with L_{Box} = 16 nm remains positive for at least 20 ps. Of course, these time values are subject to large uncertainties because of the statistical noise. Nevertheless, we could compare these values by estimating the hydrodynamic correlation time $t_H = L_{Box}/v_T$, where v_T is the velocity of thermal motion (sound velocity) based on the equipartition theorem, $k_BT = m\langle v_T^2 \rangle$. For the simulation box with L_{Box} = 4 nm, t_H is about 8.7 ps, while it is around 17.5 ps for L_{Box} = 8 nm and 35.1 ps for L_{Box} = 16 nm. The estimated t_H values are fairly similar to the times for the VACFs to first reach negative values. This again reflects the existence of hydrodynamic correlations in our simulations using periodic boundary conditions.

Because the diffusion coefficient is the time integral of the VACF, the results in Fig. A5.1(b) are consistent with the simulation work of Yeh and Hummer [61], where the diffusion coefficients increase with system size. However, our data for directional motion are not affected by this effect. The characteristic hydrodynamic correlation times are all longer than the time required for the drift to reach the saturation value. We thus believe that the finite size effect originating from the hydrodynamic correlations between particles in neighboring boxes does not have a strong effect on the directional motion behavior we are interested in, as least not qualitatively as shown in Fig. A5.1(a). This could be understood by considering the physical origin of the drift behavior, for which the effective driving force results from the imbalanced collision forces with solvent molecules during the rotation of the particle. As illustrated in Fig. A5.1(c), the positive driving force only lasts for about 1 ps and the remaining part of the drift process is caused by inertia along the initial driving direction. The hydrodynamic correlations therefore have no effect on the origin of the drift, as evidenced in Fig. A5.1(c). They may potentially affect the magnitude of the drift, but this is not the case in Fig. A5.1(a).

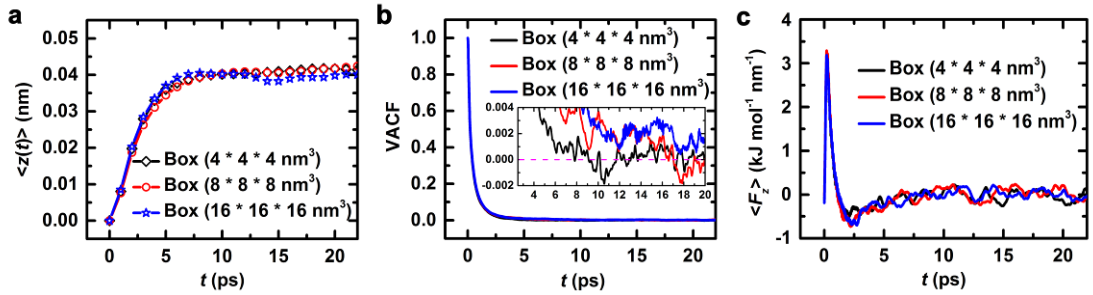

Figure A5.1 (a) Time-dependent directional drift, (b) velocity autocorrelation function, and (c) mean force projected on the z-axis of a model particle with height h = 0.37 nm solvated in simulation boxes of side lengths L_{Box} of 4, 8, and 16 nm. The inset in (b) is an enlarged view around zero.